https://doi.org/10.1016/j.ijhydene.2019.10.139

3D thermo-electro-chemo-mechanical coupled modeling of solid oxide fuel cell with double-sided cathodes

Congying Jiang[a,b], Yuchen Gu[a,b], Wanbing Guan[b,*], Jiahong Zheng[a,b], Meng Ni[c], Zheng Zhong[a,d*]

[a] School of Aerospace Engineering and Applied Mechanics, Tongji University, Shanghai 200092, China

[b] Ningbo Institute of Material Technology and Engineering, Chinese Academy of Sciences, Ningbo 315201, China

[c] Department of Building and Real Estate, The Hong Kong Polytechnic University, Hung Hom, Kowloon, Hong Kong SAR, China

[d] School of Science, Harbin Institute of Technology, Shenzhen 518055, China

Abstract

A solid oxide fuel cell based on double-sided cathodes is developed in our group, showing special properties and much advantages under some harsh conditions. To optimize the cell further, a thermo-electro-chemo-mechanical coupled 3D model is developed to simulate the distributions of temperature, current density, fuel gas and thermal stress under different voltages. The numerical results indicate that the temperature distribution, current, fuel gases and thermal stress is non-uniform in the cell at different voltages. The distribution of thermal stress in the electrolyte is also non-uniform because of the un-even electrochemical reaction and convective heat transfer.

* Corresponding author.

Email address: W.B. Guan, wbguan@nimte.ac.cn;zhongzheng@hit.edu.cn

Furthermore, the result shows that about 47%~54% maximum 1st principal stress in SOFC is caused by the mismatch of coefficients of thermal expansion(CTEs) among materials, while the other part of the maximum 1st principal stress is mainly caused by temperature gradient.

Keywords: Solid oxide fuel cell (SOFC); Multi-physics model; Thermal stress; Temperature gradient; 1st principal stress

1 Introduction

Solid Oxide Fuel Cell (SOFC) is a highly efficient, environmental friendly and fuels flexible power generation device, which has a promising application in the future [1, 2]. SOFCs are categorized into two major types as planar and tubular configurations. Tubular SOFCs have been assessed to be more secure than the planar designed since they can be easily sealed [3]. While, the most commercially available system demonstrated is made by the planar configuration due to manufacturing considerations, optimal volumetric power density [4, 5]. For the traditional anode-supported planar cells, the mismatch of coefficients of thermal expansion (CTEs) between materials in each layer may give rise to thermal stress during operation, resulting in cracks of ultra-thin electrolytes, and ultimately leading to operational damages and performance degradation [6, 7]. As researched by Guan et al. [8, 9], when the stack is short (such as

three-cell stack), the temperature distribution is relative uniform, while the temperature distribution is un-even for the stack modula and stack series as the discharging current is more than a certain value. The uneven temperature will cause the thermal stress even the proper materials was chosen at the operating temperature as reported by Chiang et al. [10]. To remit or overcome this defect, a flat-tube SOFC based on double-sided cathodes is proposed and evaluated recently [11, 12], as shown in Fig.1. For this double-sided cathode structure, deformation introduced by thermal stress is partially offset because of its completely symmetric structure. In order to further improve the cell performance, an in-depth understanding of the distributions of temperature, current, fuel gas and thermal stress in this newly structure is needed.

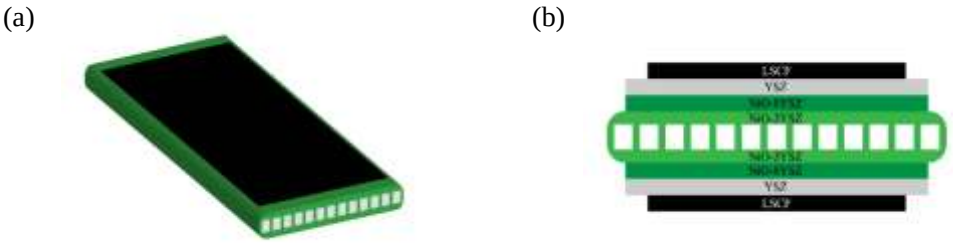

Fig. 1 Geometry of designed SOFC with double-sided cathodes (a) schematic diagram, (b) schematic of components

Compared with the experiment, numerical simulation is an easier, economic and time-saving method, and was widely used to improve cell performance [13-15]. Some researches focused on performance improvement, the heat/mass transfer and electrochemical reaction effects have been coupled in models, while the thermal stress

is generally ignored [16,17]. Some publications focused on the cell durability and reliability, thermal mechanical behavior was studied without considering the change of voltage or flow condition [18-20]. But in fact, the thermal stress in SOFC is dependent of cell performance, and can be analyzed by a thermo-electro-chemo-mechanical coupled theoretical model. Jiang et al. [21] investigated the thermal stress in a unit cell by exporting the cell temperature predicted by a finite-volume model to a finite-element model. Numerical results showed that the thermal stress was underestimated by 46% with the assumption of a uniform temperature. Xu et al. [22] have numerically examined the thermal stress of anode-supported planar SOFC with different interconnect designs. It was found that the thermal stress can be reduced through structural correlations and wider interconnect of anode side. Zeng et al. [23] found that the increase of active sites could increase the thermal stress although it facilitates the electrochemical reactions. It could see that the researches mentioned above were mainly focused on the thermal stress in a single cell. To research the distribution of thermal stress in a SOFC stack, Peksen et al. [6, 24] introduced a transient, coupled 3D computational fluid dynamics/computational solid mechanics model, and analyzed the stress, creep strain and damage. In 2018, Fang et al. [25] calculated the thermal stress and creep strain in a SOFC stack, and failure probability of SOFCs was predicted through Weibull approach. The reference reported is mainly focused on the planar structure or tubular structure. As to our newly designed SOFC structure, it is also significant to develop a thermo-electro-chemo-mechanical coupled 3D theoretical model to simulate the distribution of temperature, current, gas flow and thermal stress.

In this work, a finite element model for the SOFC based on double-sided cathodes is established. The temperature profiles of the cell under different voltages are calculated by the thermal electrochemical model, and the distribution of thermal stress is evaluated. The iso-thermal model is also established to calculate thermal stress caused by CTEs. The simulation results can provide more information on the distributions of temperature, current density, fuel gas and stress in the double-sided cathodes SOFC, which is much useful for the cell improvement further. Simulations are carried out by the Comsol multiphysics computer software.

2 Model description

2.1 Geometry

As the double-sided cathodes SOFC is symmetric (Fig. 2a), only half of the cell is included for this simulation. This model consists of 26 metallic alloy interconnect tips (1.15mm × 28mm × 1mm), an air channel, a $La_{0.6}Sr_{0.4}Co_{0.2}Fe_{0.8}O_{3-\delta}$(LSCF) perovskite cathode active layer (85.5mm × 41mm × 0.02mm), a yttria-stabilized zirconia (YSZ) electrolyte layer (85.5mm × 41mm × 0.01mm), a NiO+8YSZ anode active layer (85.5mm × 41mm × 0.02mm), a NiO+3YSZ anode support layer and 13 fuel gas channels (98.6mm × 2.5mm × 2.3mm), as shown in Fig. 2b. The schematic geometry of SOFC is shown in Fig. 2c. To illustrate the flow of air clearly, the geometry of air channel is given in Fig. 2d. There are total 81423 grids and 32469 nodes in this model.

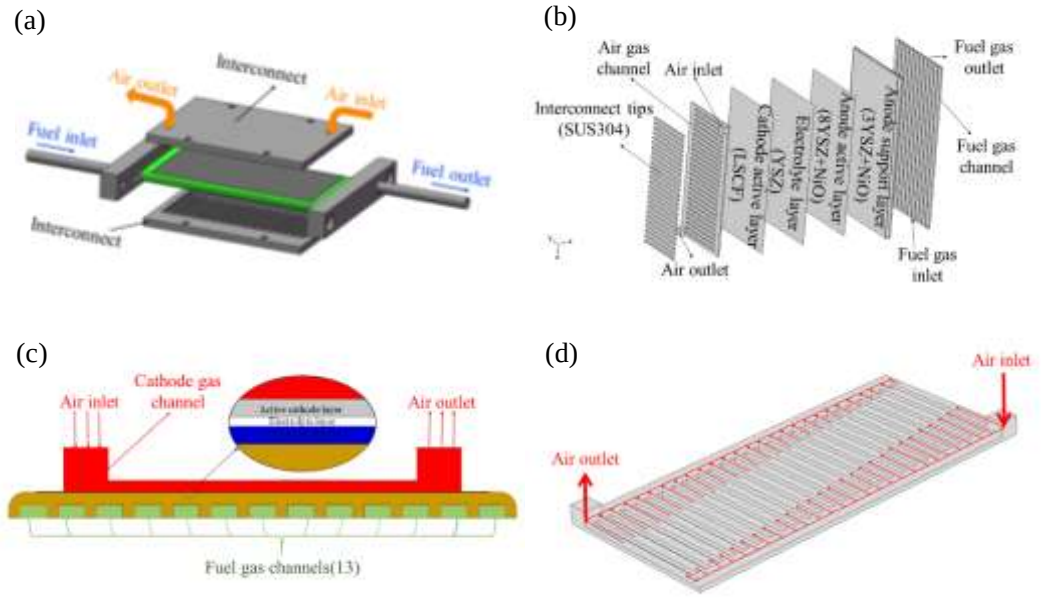

Fig. 2 Geometry of double-sided cathodes SOFC: (a) schematic of assembly system, (b) components of SOFC, (c) overall geometry and (d) air gas channel.

2.2 Governing equations

The 3D thermo-electro-chemo-mechanical coupled numerical model fully considers the electrochemical reactions, gases flow, species diffusion, heat transfer and solids deformation processes. To present these processes clearly, it is necessary to couple electrochemical reaction models, gas flow models, species diffusion models, heat transfer model and mechanical model together. The governing equations of these models are presented as follow.

2.2.1 Electrochemical reaction models

Hydrogen oxidation in active anode layer is considered in this work as expressed as:

$$H_2 + O^{2-} \rightarrow H_2O + 2e^- \quad (1)$$

where H_2 is supplied by fuel channel and $O^{2-}$is produced in cathode and transmitted into anode through electrolyte. In cathode, one mole O_2 accommodate four moles of electrons at the surface area of LSCF which is exposed to air, as shown in Eq. (2):

$$O_2 + 4e^- \rightarrow 2O^{2-} \quad (2)$$

The operating cell potential (E) from the SOFC can be determined using the equilibrium potential and the various over potential losses:

$$E = \mathrm{E}^{\mathrm{OCV}} - \left(\eta_{\mathrm{act}} + \eta_{\mathrm{ohm}} + \eta_{\mathrm{conc}}\right) \quad (3)$$

Where $\mathrm{E}^{\mathrm{OCV}}$ is the equilibrium potential (Nernst potential) when the current density is zero. η_{act}, η_{ohm} and η_{conc} are activation, ohmic and concentration overpotentials respectively. For the hydrogen-steam mixture fuel, the equilibrium potential can be calculated by the Nernst equation with the stand electrode potential E^0, universal gas constant R, temperature T, pressure p, Faraday's constant F and referential concentration of component i (c^i_{ref})[26]:

$$E^{\mathrm{OCV}} = E^0 + \frac{\mathrm{R}T}{2\mathrm{F}} \ln\left(\frac{c_{ref}^{\mathrm{H_2}}\left(c_{ref}^{\mathrm{O_2}}\right)^{0.5}}{c_{ref}^{\mathrm{H_2O}}}\right) + \frac{\mathrm{R}T}{4\mathrm{F}} \ln p \quad (4)$$

In addition, the stand electrode potential E^0 can be expressed as [23]:

$$E^0 = 1.253 - 2.4516 \times 10^{-4} T \quad (5)$$

The activation polarization/current density relationships in anode and cathode are

described by the Butler-Volmer (BV) equations, in which both η_{act} and η_{conc} are considered [22, 27, 28]:

$$\text{Anode}: \quad i^a = \mathrm{S}^a_{\text{TPB}} i^a_0 \left[\frac{c^{\mathrm{H_2}}}{c^{\mathrm{H_2}}_{ref}} \exp\left(\frac{\alpha^a \mathrm{n}^a \mathrm{F}\left(\eta^a_{\text{act}} + \eta^a_{\text{conc}}\right)}{\mathrm{RT}} \right) - \frac{c^{\mathrm{H_2O}}}{c^{\mathrm{H_2O}}_{ref}} \exp\left(\frac{\left(1-\alpha^a\right) \mathrm{n}^a \mathrm{F}\left(\eta^a_{\text{act}} + \eta^a_{\text{conc}}\right)}{\mathrm{RT}} \right) \right]$$

$$\text{Cathode}: \quad i^c = \mathrm{S}^c_{\text{TPB}} i^c_0 \left[\exp\left(\frac{\alpha^c \mathrm{n}^c \mathrm{F}\left(\eta^c_{\text{act}} + \eta^c_{\text{conc}}\right)}{\mathrm{RT}} \right) - \frac{c^{\mathrm{O_2}}}{c^{\mathrm{O_2}}_{ref}} \exp\left(\frac{\left(1-\alpha^c\right) \mathrm{n}^c \mathrm{F}\left(\eta^c_{\text{act}} + \eta^c_{\text{conc}}\right)}{\mathrm{RT}} \right) \right] \tag{6}$$

where, i_0 is the exchange current density (unit), α^a and α^c are the electronic transfer coefficients of anode and cathode, n is the number of electrons transferred per electrochemical reaction and $\mathrm{S_{TPB}}$ (unit) is the density of length of triple phase boundary (TPB), the superscript a and c represent anode and cathode respectively. c^i is the concentration of component i.

The ohmic overpotential in SOFC is caused by the transfer of ion or electron. The governing equations for the transport of electron and ion can be expressed as:

$$\begin{aligned} \mathbf{i}_i &= -\sigma^e_i \nabla \Phi_i \\ \mathbf{i}_e &= -\sigma^e_e \nabla \Phi_e \end{aligned} \tag{7}$$

where **i**, σ^e and **Φ** are the current, conductivity and electric potential, respectively. The subscript **i** and e represent ion and electron respectively, and ∇ is gradient operator. The parameters used in these electrochemical reaction models are summarized in table 1 as [7, 17, 29-31]:

Table 1. Parameters for the electrochemical reaction model

Parameters	Value
Ionic conductivity of anode ($S \cdot m^{-1}$) [7,29]	$\frac{9.5\times10^{7}}{T}\exp\left(-\frac{1150}{T}\right)$
Ionic conductivity of cathode ($S \cdot m^{-1}$)[7,29]	$\frac{4.2\times10^{7}}{T}\exp\left(-\frac{1200}{T}\right)$ [7,18]
Ionic conductivity of electrolyte ($S \cdot m^{-1}$)[7,29]	$33.4\times10^{3}\exp\left(-\frac{10300}{T}\right)$ [7,18]
Electronic conductivity of anode($S \cdot m^{-1}$) [17]	30300
Electronic conductivity of cathode($S \cdot m^{-1}$) [17]	17000
Electronic conductivity of interconnect($S \cdot m^{-1}$) [17]	769000
S_{TPB}^{a} ($m \cdot m^{-3}$) [30,31]	2.14×10^{5}
S_{TPB}^{c} ($m \cdot m^{-3}$) [30,31]	2.14×10^{5}
α^{a} [30,31]	0.5
α^{c} [30,31]	0.5
$i_0{}^{a}$ ($A \cdot m^{-1}$)	630
$i_0{}^{c}$ ($A \cdot m^{-1}$)	60

From the table 1, it can be seen clearly that the electronic conductivity of anode and cathode are much higher than that of the electrolyte. Thus, the effect of the

electronic conductivity of the anode and cathode on the distribution of multi-physics fields could be ignored. Thus, the electronic conductivity could be assumed as temperature and oxygen partial pressure independent.

2.2.2 Gas flow models

The gases can flow between electrodes and gas channels freely. The fluid flow in porous electrodes and gas channels could be simulated together. However, the governing equations are different for electrodes and channels. To describe the momentum conservation in porous electrodes, the widely used Navier-Stokes equation is modified by introducing Darcy's term and the porosity is also considered [28, 32]:

$$\begin{aligned} &\nabla\cdot\left(\rho\mathbf{v}\right)=S_{mass}\\ &\rho\mathbf{v}\cdot\nabla\mathbf{v}=-\nabla p+\nabla\cdot\left[\mu\left(\nabla\mathbf{v}+\mathbf{v}\nabla\right)-\frac{2}{3}\mu\nabla\mathbf{v}\right]-\frac{\varepsilon\mu\mathbf{v}}{k}\\ &\text{Anode}: \qquad S_{mass}=\frac{\left(M_{H_2O}-M_{H_2}\right)i}{2\mathrm{F}}\\ &\text{Cathode}: \qquad S_{mass}=-\frac{M_{O_2}i}{4\mathrm{F}} \end{aligned} \tag{8}$$

where $\mathbf{v}$ is the velocity vector, S_{mass} is the mass source term, $\boldsymbol{\varepsilon}$ is the porosity and k is specific permeability which depends on the geometry of the porous medium. In gas channels, the flow of gases is not related with porosity, and the Darcy's term are neglected. The governing equations can be expressed as:

$$\begin{aligned} &\nabla\cdot\left(\rho\mathbf{v}\right)=S_{mass}\\ &\rho\mathbf{v}\cdot\nabla\mathbf{v}=-\nabla p+\nabla\cdot\left[\mu\left(\nabla\mathbf{v}+\mathbf{v}\nabla\right)-\frac{2}{3}\mu\nabla\mathbf{v}\right] \end{aligned} \tag{9}$$

In addition, ρ and μ are the total gas density and gas dynamic viscosity which are

dependent on the component of gas. The values of ρ and μ are calculated with the following equations [33]:

$$\rho = \frac{p\sum x_i M_i}{\mathrm{RT}} \tag{10}$$

$$\mu = \sum x_i \mu_i \tag{11}$$

where x_i, M_i and μ_i are the mole fraction, molecular weight and dynamic viscosity of component i. To get these three parameters, the species diffusion models are needed in the next section. For the electrolyte in SOFC, the fluid flow could be neglected because it is full dense, and gas can't pass through freely.

2.2.3 Species diffusion models

The electrochemical reactions happen near the interface of electrolyte and electrodes [34]. To reach the reaction sites, gases must diffuse through the gas-filled pores of the electrode. The pores in active anode layer are small in comparison with the mean free path of the gas, which means that molecules collide more frequently with the pore surfaces and Knudsen diffusion plays an important role in diffusion [35]. Thus, the general Fick's law which combines Knudsen diffusion and Fick's laws is employed in species diffusion models:

$$\mathbf{j}_i = -\rho \mathrm{D}_i^{mk} \nabla \omega_i - \rho \omega_i \mathrm{D}_i^{mk} \frac{\nabla M}{M} + \rho \omega_i \sum_k \frac{M_i}{M} \mathrm{D}_k^{mk} \nabla x_k \tag{12}$$

$$\mathrm{D}_i^{mk} = \frac{\varepsilon}{\tau}\left(\frac{1}{\mathrm{D}_i^m} + \frac{1}{\mathrm{D}_i^k}\right)^{-1} \tag{13}$$

$$M = \left(\sum_i \frac{\omega_i}{M_i} \right)^{-1} \tag{14}$$

Here, w_i is mass fraction of specie i, $\boldsymbol{j}_i$ is the mass flux of species i, ε is the volume fraction of the pores, τ is the tortuosity factor, M is total molar mass, D^{mk} is total diffusion coefficient of species which can be calculated by Fick's diffusion coefficient (D^m) and Knudsen's diffusion coefficient (D^k) [36, 37].

In addition, for the species diffusion models, the conservation of mass is:

$$\begin{aligned} &\nabla \cdot \mathbf{j}_i + \rho\left(\varepsilon \mathbf{v} \cdot \nabla\right)\omega_i = S_i \\ &S_{H_2} = M_{H_2} \frac{i}{2\mathrm{F}} \\ &S_{H_2O} = -M_{H_2O} \frac{i}{2\mathrm{F}} \\ &S_{O_2} = M_{O_2} \frac{i}{4\mathrm{F}} \end{aligned} \tag{15}$$

In which S_i is the mass source term of component i which is produced or consumed by electrochemical reaction per second per volume. The change of materials in quantity caused by diffusion(first term), convection(second term) and reaction(third term) are all taken into consideration in Eq. (15).

2.2.4 The heat transfer model

The classical heat transfer governing equation is:

$$\rho \mathrm{C}_p \mathbf{v} \cdot \nabla T = \nabla\left(\lambda_{eff} \nabla T\right) + Q \tag{16}$$

where C_p is the specific heat capacity, and Q is the heat source term in the cell. λ_{eff} is the effective thermal conductivity which is determined by the components of gases in

gas channels. While the λ_{eff} of the porous electrode is calculated as

$$\lambda_{eff} = (1-\varepsilon)\lambda_s + \varepsilon\lambda_g \tag{17}$$

where λ_s and λ_g are the thermal conductivity of gases and solids.

In this model, an assumption is made that the heat source is introduced by Joule effect of ions and electrons:

$$Q=\sigma_i^e \nabla\Phi_i \cdot \nabla\Phi_i + \sigma_e^e \nabla\Phi_i \cdot \nabla\Phi_i \tag{18}$$

The parameters used in these gas flow, species diffusion and heat transfer models are presented in table 2 [38]as:

Table 2. Parameters and values used in the heat and mass transfer models

Parameters	Porosity	Permeability (m^2)	Thermal Conductivity ($W \cdot m^{-1} \cdot K^{-1}$)	Thermal capacity ($W \cdot Kg^{-1} \cdot K^{-1}$)
Anode active layer [38]	0.23	1×10^{-12}	6	450
Anode support layer [38]	0.46	1×10^{-10}	6	450
Electrolyte [38]	-	-	2.7	550
Cathode layer [38]	0.3	1×10^{-12}	11	430

Interconnect [38]	-	-	20	550

2.2.5 The mechanical model

The mechanical model in this work assumes that solid materials in SOFC are elasticity, and the deformation caused by thermal stress is small. The traditional three-dimensional governing equations can be sorted into three types of equations as [39]:

$$\begin{aligned} &\text{Geometric equation} && \boldsymbol{\varepsilon}=\left(\nabla\mathbf{u}+\mathbf{u}\nabla\right)/2 \\ &\text{Momentum equation} && \nabla\cdot\boldsymbol{\sigma}+\mathbf{f}=0 \\ &\text{Constitutive equation} && \boldsymbol{\sigma}=\mathbf{C}:\left(\boldsymbol{\varepsilon}-\boldsymbol{\varepsilon}_{th}\right) \end{aligned} \tag{19}$$

where $\boldsymbol{\varepsilon}$ and $\boldsymbol{\sigma}$ are two-order tensors which represent total strain and stress respectively. $\boldsymbol{\varepsilon}_{th}$ is the thermal strain. $\mathbf{u}$ is the displacement. $\mathbf{f}$ is body force and $\mathbf{C}$ is a fourth-order elastic coefficient tensor. For the isotropic materials, the constitutive equation in Eq. (19) can be simplified as:

$$\begin{bmatrix} \sigma_{xx} \\ \sigma_{yy} \\ \sigma_{zz} \\ \tau_{xy} \\ \tau_{xz} \\ \tau_{yz} \end{bmatrix} = \frac{\mathrm{E}}{(1+\nu)(1-2\nu)} \begin{bmatrix} 1-\nu & \nu & \nu & 0 & 0 & 0 \\ \nu & 1-\nu & \nu & 0 & 0 & 0 \\ \nu & \nu & 1-\nu & 0 & 0 & 0 \\ 0 & 0 & 0 & \frac{1-2\nu}{2} & 0 & 0 \\ 0 & 0 & 0 & 0 & \frac{1-2\nu}{2} & 0 \\ 0 & 0 & 0 & 0 & 0 & \frac{1-2\nu}{2} \end{bmatrix} \begin{bmatrix} \varepsilon^{e}_{xx} \\ \varepsilon^{e}_{yy} \\ \varepsilon^{e}_{zz} \\ \gamma^{e}_{xy} \\ \gamma^{e}_{xz} \\ \gamma^{e}_{yz} \end{bmatrix} \tag{20}$$

where E and ν are Young's modulus and Poisson's ratio respectively. ε^{e}_{xx}, ε^{e}_{yy}, ε^{e}_{zz}, γ^{e}_{xy}, γ^{e}_{xz}, γ^{e}_{yz} are the longitudinal and shear components for elastic strain. σ_{xx}, σ_{yy}, σ_{zz}, τ_{xy}, τ_{xz},

τ_{yz} are the longitudinal and shear components for stress.

In the thermo-mechanical problem, the thermal strain ($\boldsymbol{\varepsilon}_{th}$) depends on the temperature and CTE with the assumption of isotropic is:

$$\boldsymbol{\varepsilon}_{th} = \alpha\left(T - T_{ref}\right)\mathbf{I} \tag{21}$$

Here, T_{ref} (1023K) is the reference temperature, **I** is a two order unit tensor. In general, the thermal stress has the lowest value before the cell heating. However, it can be known that the cell will generate and accelerate creep during the reduction after heating, and thus the thermal stress in the half-cell (support, fuel electrode and electrolyte) will be relaxed and practically goes to zero [40, 41]. In this work, the thermal stress is assumed to be zero at 1023K, accordingly. The parameters used in this mechanical model are given in table 3 [42, 43] as:

Table 3. The parameters used in this mechanical model

Layer	Young's modulus (GPa)	Poisson's ratio	CTE ($10^{-6}K^{-1}$)
Anode active layer [42, 43]	220	0.3	12.2
Anode support layer [42, 43]	213	0.3	12.2
Electrolyte [42, 43]	205	0.3	10.3

Cathode layer [42, 43]	30	0.3	12.5
Interconnect [42, 43]	205	0.3	12.3

To simulate the SOFC under working conditions, it is necessary to choose proper boundary conditions. In this work, the laminar flow profile is specified at the gas inlet, and the average flow velocities are calculated under different gas flow rates. As for the gas outlet, the pressure is fixed at 1 atm (1.013×10^5 Pa). In addition, the fuel inlet fraction is defined as 3% H_2O (mole fraction) and 97% H_2. The gas in cathode is defined as oxygen (21%, mole fraction) and nitrogen (79%, mole fraction). To simulate the SOFC under the real condition, the initial, boundary and gas inlet temperature are set as 1023K. The potential at the anode current collector is zero, while the one at the cathode connector varies from 1.15 V to 0.3 V.

3 Results and discussion

3.1 Model evaluation

To valid our model, the results of current-potential (I-V) characteristics and power density obtained in simulation are presented and compared with experimental data as shown in Fig.3. It can be seen that the simulation results agree both qualitatively and quantitatively well with the experimental data even the voltage is lower than 0.5V.

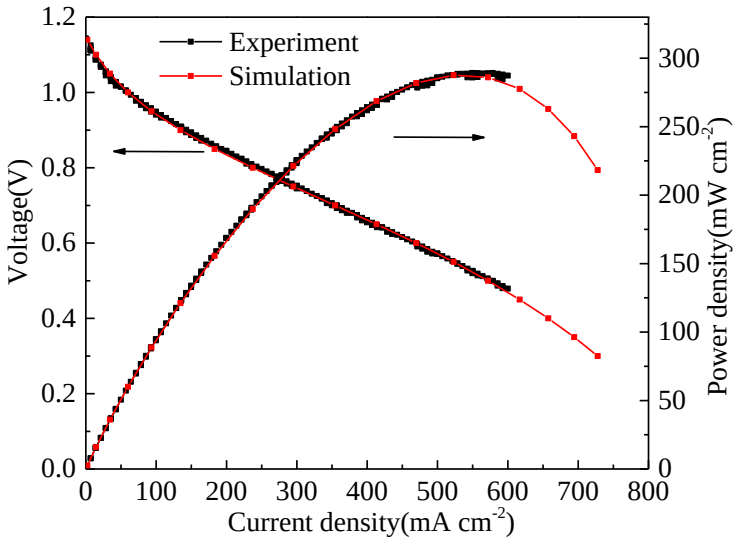

Fig. 3 I-V characteristics and power density.

3.2 Mole fraction distribution of gases in SOFC

The mole fractions of hydrogen in the middle of active anode (10 μm from the interface of anode and electrolyte) and oxygen in the middle of cathode layer (10 μm from the interface of cathode and electrolyte) at different operation voltages are illustrated in Fig.4-5. It is noted that the color legend is kept the same for all cases. Based on Fig.4, the hydrogen concentration decreases along the anode flow direction due to the continuous electrochemical reaction (along with x axis). In addition, with decreased voltage, the gradient of mole fraction of hydrogen in x direction become larger because of faster electrochemical reaction. When the voltage is 1V, the difference of maximum and minimum mole fractions of hydrogen is only 8%. However, when the voltage reaches 0.4V, the mole fraction of hydrogen in active anode ranges from 68% (near the inlet) to 4% (close to outlet). As for the oxygen in cathode shown in Fig 5, the distribution of mole fraction becomes more non-uniform because of the complicated

geometry of cathode gas channel. Firstly, the interconnection tip directly isolates the contact between the gas and the cathode layer. Thus, it is harder for the oxygen to reach these areas and the mole fraction of oxygen in these areas is smaller compared with these exposed to air. Secondly, because of the unique design of cathode gas channel which is different from traditional cross-flow or counter-flow configuration, the velocity of air in cathode gas channel is non-uniform as shown in Fig. 6. The velocity of air in the middle area (low velocity area in Fig.6) is small, and the oxygen consumed by electrochemical reaction can't be supplied by convection immediately. Thus, the mole fractions of oxygen in cathode layer near low velocity gas channel is much smaller compared with other areas, especially at a low voltage.

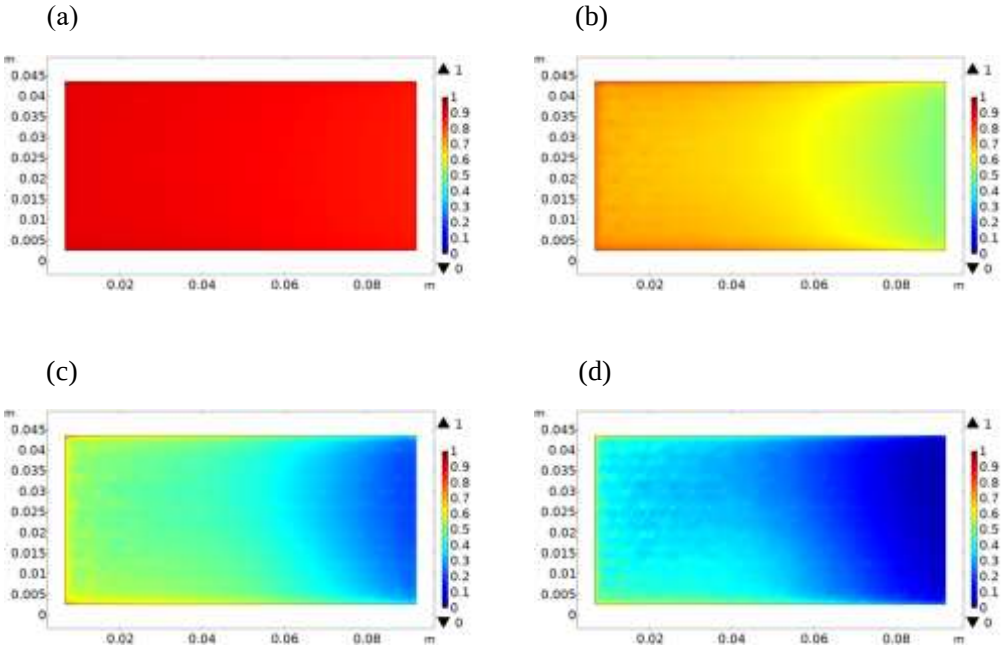

Fig. 4 Mole fractions of hydrogen in active anode with different operation voltages: (a) V_{cell}=1V, (b) V_{cell}=0.8V, (c) V_{cell}=0.6V, (d) V_{cell}=0.4V.

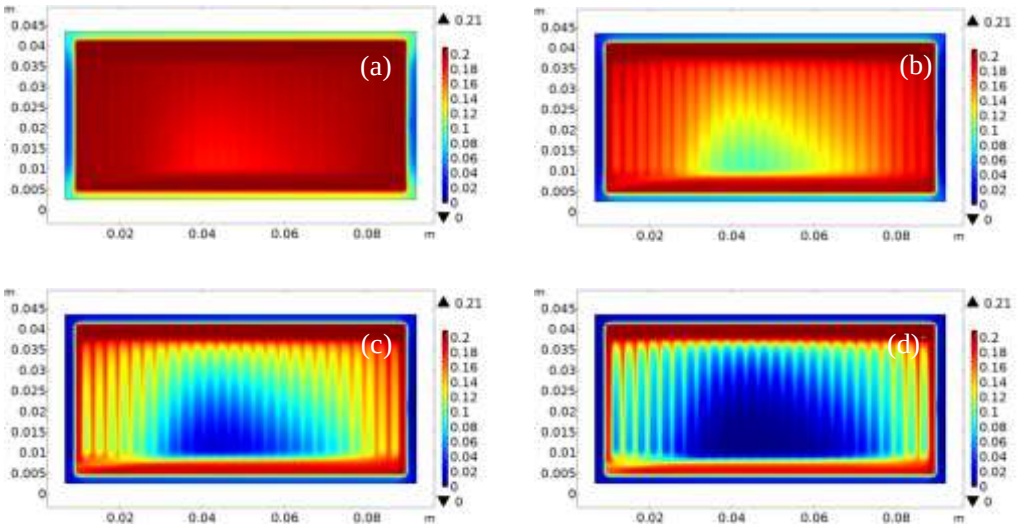

Fig. 5 Mole fractions of oxygen in cathode layer with different operation voltages: (a) V_{cell} =1V, (b) V_{cell}=0.8V, (c) V_{cell}=0.6V, (d) V_{cell}=0.4V.

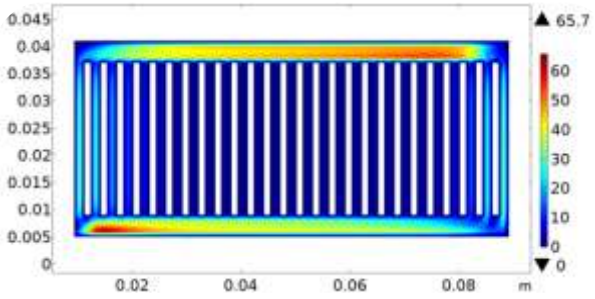

Fig. 6 Velocity of air in cathode gas channel (V_{cell}=1V).

3.3 Distribution of current density in electrolyte

The current density in electrolyte is dominated by the rate of electrochemical reaction which is influenced by the voltage, density of the TPB length, partial pressure of hydrogen, oxygen and water, as expressed in Eq. (6). Thus, as presented in Fig.7, when the voltage is decreased from 1V to 0.4V, the current density in electrolyte is increased significantly. Moreover, the current density in electrolyte is also low for the area where the concentration of oxygen is low in cathode, as shown in Fig. 5.

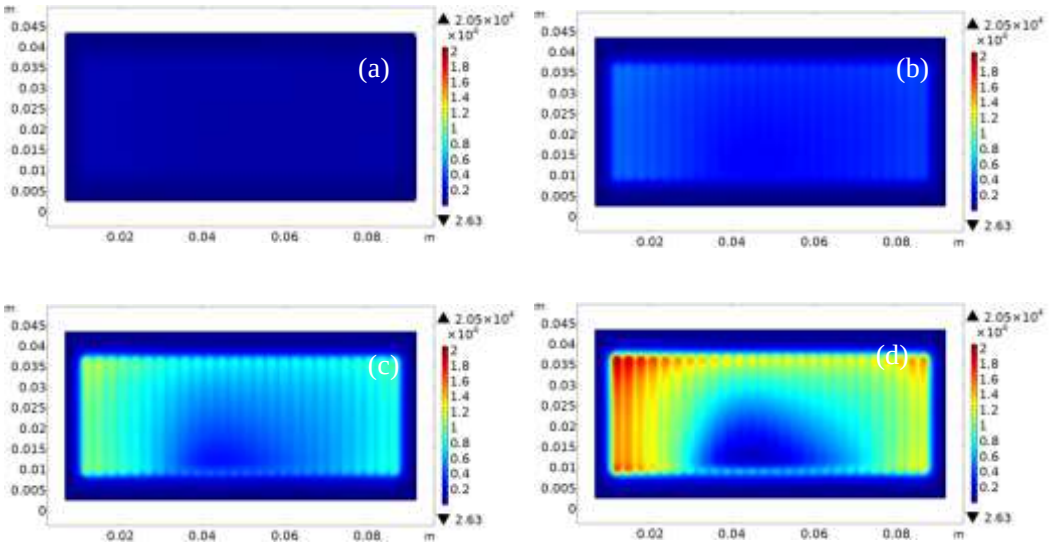

Fig. 7 Distribution of current density in electrolyte with different operation voltages: (a) V_{cell}=1V, (b) V_{cell}=0.8V, (c) V_{cell}=0.6V, (d) V_{cell}=0.4V.

3.4 Distribution of temperature in electrolyte

To investigate the distribution of thermal stress in SOFC, the profiles of temperature in SOFC electrolyte are calculated and shown in Fig.8. The temperature increases rapidly because of the electrochemical reaction and ohmic heat. The high temperature zone located at the lower left corner near the outlet of air and inlet of hydrogen. The temperature differences are 4°C, 37°C, 112°C and 222°C under the voltage of 1V, 0.8V, 0.6V and 0.4V, respectively. The relation between average or highest temperature and voltage in electrolyte is non-linear, as illustrated in Fig. 9. The peak temperature at 0.3V is more than 250°C higher than that at an equilibrium potential. In all, the temperature distribution is non-uniform, especially at a low voltage, which may cause local thermal stress and lead to cell failure.

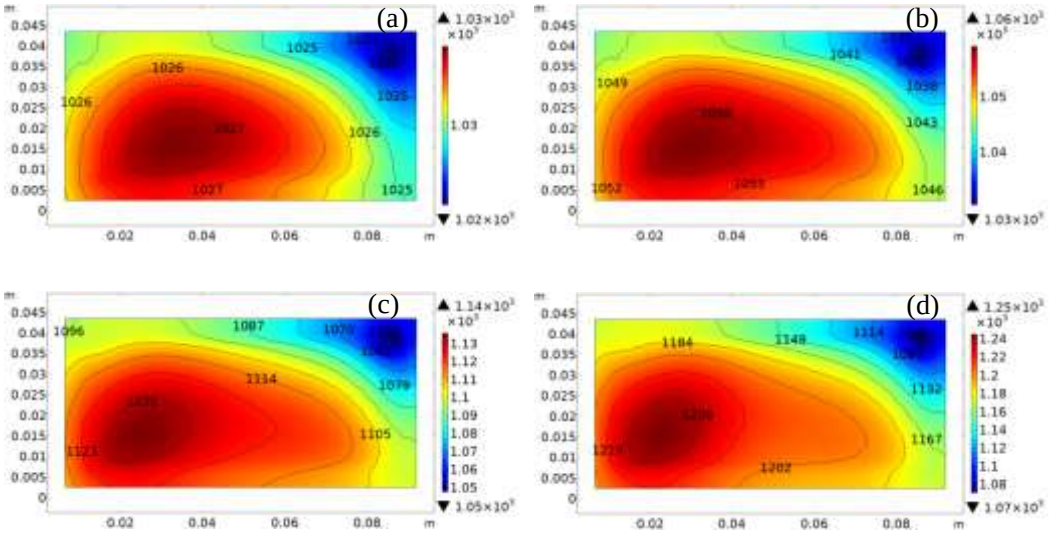

Fig. 8 Distribution of temperature in electrolyte with different operation voltages:(a) V_{cell} =1V, (b) V_{cell} =0.8V, (c) V_{cell} =0.6V, (d) V_{cell} =0.4V.

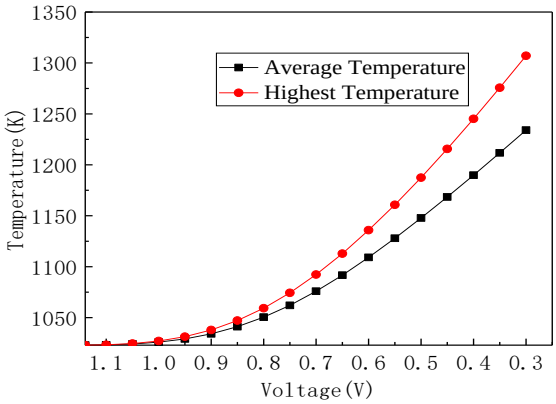

Fig. 9 Average and highest temperature at different voltage in electrolyte.

3.5 Distribution of stress in SOFC

The 1st principal stress is normally the maximum stress normal to a plane which may induce thermal crack in ceramic cell, and is always used to predict the lifetime of a cell. The distribution of the 1st principal stress at different voltages is shown in Fig. 10. It shows that the 1st principal stress in electrolyte is much higher than that in anode and cathode (especially when the voltage is low) because of low CTE. And thus, the

electrolyte is more easy to fail because of its high thermal stress [7]. The distribution of 1st principal stress in electrolyte is shown in Fig. 11. The maximum 1st principal stress in electrolyte ranges from 3.51 MPa to 177 MPa when voltage decreases from 1V to 0.4V. It is because that a lower voltage leads to a higher temperature and a higher thermal deformation. Moreover, the distribution of stress in electrolyte is non-uniform, and its maximum 1st principal stress is 6.62, 5.17, 4.56 and 4.56 times the value of the lowest one at the voltage of 1V, 0.8V, 0.6V and 0.4V. The non-uniform distribution of stress is mainly caused by non-uniform temperature distribution.

In fact, the maximum 1st principal stress in electrolyte is influenced by both temperature and temperature gradient. When the voltage is 1V, 0.8V, 0.6V and 0.4V, the maximum temperature is 1027K, 1059K,1136K and 1245K, with the corresponding maximum 1st principal stress of 3.51 MPa, 30.5 MPa, 92.1MPa and 177 MPa, respectively. For comparison, an iso-thermal model was also developed with uniform temperature (1027 K, 1059 K,1136 K and 1245 K). And only the thermal and mechanical fields are considered in the new model. The distribution of stress is shown in Fig.12. and the maximum 1st principal stresses are about 2.32 MPa, 20.7 MPa, 64.5 MPa and 127 MPa. It can be seen that the distribution of 1st principal stress is more uniform with a uniform temperature distribution. Even at the maximum temperature under the voltage of 1V, 0.8V, 0.6V and 0.4V, the maximum 1st principal stresses are 34.1 %, 32.3 %, 30% and 28.7% smaller than those reported with the previous models (non-isothermal models). In addition， the maximum 1st principal stresses in SOFC at

different average uniform temperature of different voltages are presented in Fig.13. The results show that about 46%~53% maximum 1st principal stress can be eliminated, while the other part of 1st principal stress still exists because of different CTE among various materials even the SOFC is optimized well and its temperature distribution is uniform.

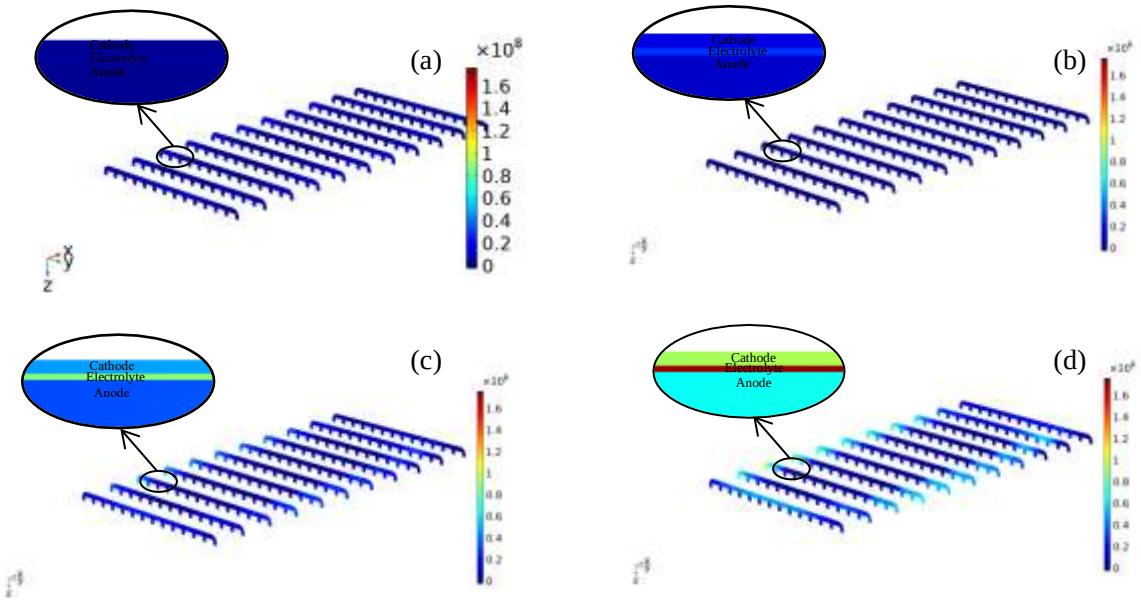

Fig. 10 Distribution of the 1st principal stress in SOFC with different operation voltages: (a) V_{cell}=1V, (b) V_{cell}=0.8V, (c) V_{cell}=0.6V, (d) V_{cell}=0.4V.

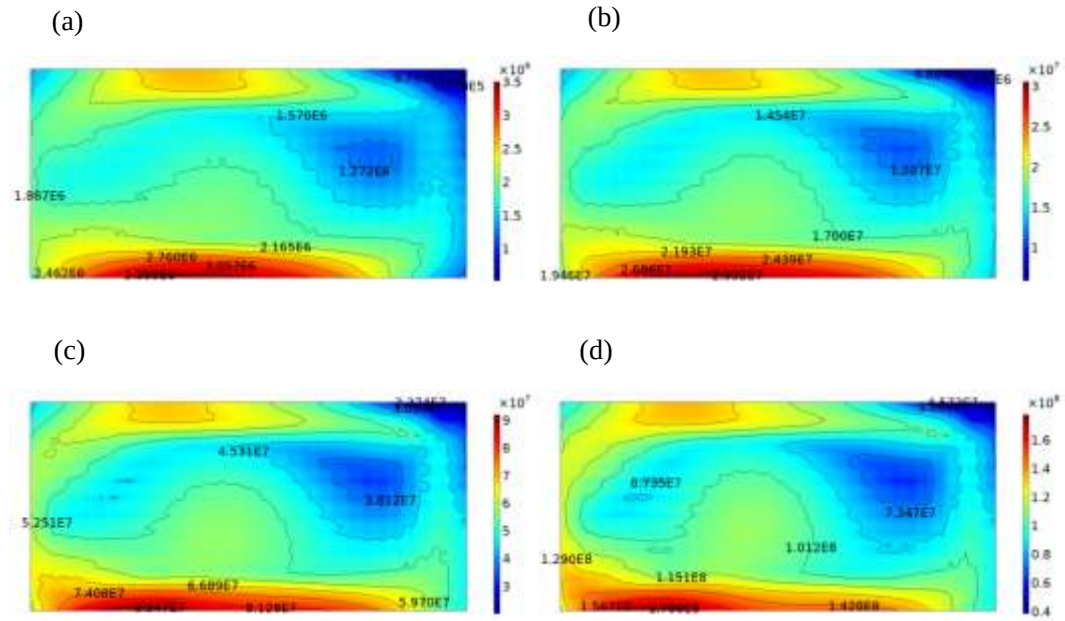

Fig. 11 Distribution of the 1st principal stress in electrolyte with different operation voltages: (a) V_{cell}=1V, (b) V_{cell}=0.8V, (c) V_{cell}=0.6V, (d) V_{cell}=0.4V.

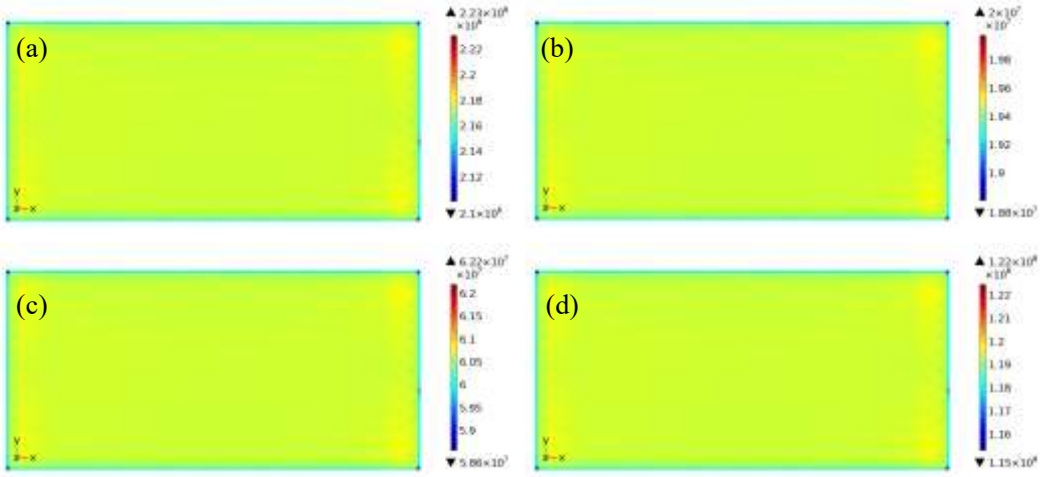

Fig. 12 The maximum 1st principal stresses in SOFC under different uniform temperature: (a) 1027 K, (b)1059 K, (c)1136 K and (d)1245 K.

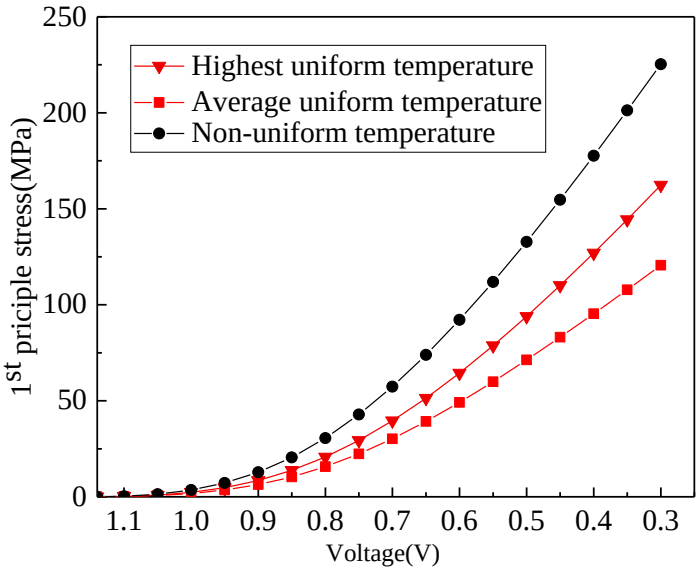

Fig. 13 The maximum 1st principal stresses in SOFC under different voltages.

4 Conclusions

A comprehensive thermo-electro-chemo-mechanical coupled 3D theoretical model has been applied to characterize the performance, temperature and stress distributions in a flat tube SOFC based on double-sided cathodes. The model is validated by comparing the results with experiment. The distributions of mole fractions of gases, current density, temperature and stress are analyzed in detail.

The mole fraction of hydrogen in active anode layer decreases along the fuel gas flow direction and the gradient becomes larger with the decrease of voltage. Different from the design of cross-flow or counter-flow configurations, the position with low oxygen mole fraction in cathode layer exists in the middle of the cell where the velocity in air channel is low. In addition, for the place where the mole fraction of oxygen is low, the current density in electrolyte is also low because of the concentration polarization.

Thus, it is necessary to redesign the configuration of cathode gas channel to make the distribution of oxygen in cathode more uniform.

The high temperature zone located at the low left corner near the outlet of air and inlet of hydrogen. The relation between average or highest temperature and voltage in electrolyte is non-linear. The lower the voltage, the larger the temperature gradient in electrolyte, and thus causes the higher thermal stress.

The 1st principal stress in electrolyte is much higher than that in anode and cathode, which indicates that the electrolyte is easier to fail under the working condition. Moreover, the distribution of thermal stress in electrolyte is non-uniform because of the un-even temperature. In this SOFC, more than 28~35% maximum 1st principal stress is caused by the temperature gradient. In addition, about 47%~54% maximum 1st principal stress is caused by different CTEs of various materials.

Acknowledgements

This work was supported by Key R&D Program from the Ministry of Science and Technology of China (No. 2018YFB1502600), and National Natural Science Foundation of China (No. 11772106, No. 51702333). Dr. Ni thanks the funding support (Project Number: PolyU 152214/17E) from Research Grant Council, University Grants Committee, Hong Kong SAR.

References

[1] Ni M, Zhao TS. Solid Oxide Fuel Cells: From Materials to System Modeling: Royal Society of Chemistry;2013.

[2] Singhal SC, Kendall K. High-temperature solid oxide fuel cells: fundamentals, design and applications: Elsevier; 2003.

[3] Sandhu NK, Hanifi AR, Woldnik A, Amiri T, Etsell TH, Luo J, et al. Electrochemical performance of a short tubular solid oxide fuel cell stack at intermediate temperatures. Appl Energy. 2016;183:358-68. https://doi.org/10.1016/j.apenergy.2016.08.179

[4] Yakabe H, Ogiwara T, Hishinuma M, Yasuda I. 3-D model calculation for planar SOFC, J Power Sources, vol. 2001;102;144-154. https://doi.org/10.1016/S0378-7753(01)00792-3

[5] Chelmehsara ME, Mahmoudimehr J. Techno-economic comparison of anode-supported, cathode-supported, and electrolyte-supported SOFCs. Int J Hydrogen Energy. 2018;43:15521-30. https://doi.org/10.1016/j.ijhydene.2018.06.114

[6] Peksen M. 3D CFD/FEM analysis of thermomechanical long-term behaviour in SOFCs: Furnace operation with different fuel gases. Int J Hydrogen Energy. 2015;40:12362-9. https://doi.org/10.1016/j.ijhydene.2015.07.018

[7] Kim YJ, Lee MC. Numerical investigation of flow/heat transfer and structural stress in a planar solid oxide fuel cell. Int J Hydrogen Energy. 2017;42:18504-13. https://doi.org/10.1016/j.ijhydene.2017.04.140

[8] Yu R, Guan W, Zhou X-D. Probing temperature inside planar SOFC short stack,

modules, and stack series. JOM. 2017;69:247-53.

[9] Guan W, Zhai H, Jin L, Xu C, Wang W. Temperature measurement and distribution inside planar SOFC stacks. Fuel cells. 2012;12:24-31.

[10] Chiang LK, Liu HC, Shiu YH, Lee CH, Lee RY. Thermal stress and thermo-electrochemical analysis of a planar anode-supported solid oxide fuel cell: Effects of anode porosity. J Power Sources. 2010;195:1895-904. https://doi.org/10.1016/j.jpowsour.2009.10.011

[11] Liu W, Zou Z, Miao F, Li X, Wang J, Yang J, et al. Anode-Supported Planar Solid Oxide Fuel Cells Based on Double-sided Cathodes. Energy Technology. 2019;7:240-4. https://doi.org/10.1002/ente.201800743

[12] Li X, Wang Y, Liu W, Wilson JA, Wang J, Wang C, et al. Reliability of CO2 electrolysis by solid oxide electrolysis cells with a flat tube based on a composite double-sided air electrode. Composites Part B: Engineering. 2019;166:549-54. https://doi.org/10.1016/j.compositesb.2019.02.012

[13] Wu C, Yang Z, Huo S, Najmi A-U-H, Du Q, Jiao K. Modeling and optimization of electrode structure design for solid oxide fuel cell. Int J Hydrogen Energy. 2018;43:14648-64. https://doi.org/10.1016/j.ijhydene.2018.05.152

[14] Amiri A, Vijay P, Tade MO, Ahmed K, Ingram GD, Pareek V, et al. Planar SOFC system modelling and simulation including a 3D stack module. Int J Hydrogen Energy. 2016;41:2919-30. https://doi.org/10.1016/j.ijhydene.2015.12.076

[15] Canavar M, Mat A, Celik S, Timurkutluk B, Kaplan Y. Investigation of temperature distribution and performance of SOFC short stack with/without machined gas channels.

Int J Hydrogen Energy. 2016;41:10030-6. https://doi.org/10.1016/j.ijhydene.2016.02.045

[16] Li X, Shi W, Han M. Optimization of interconnect flow channels width in a planar solid oxide fuel cell. Int J Hydrogen Energy. 2018;43:21524-34. https://doi.org/10.1016/j.ijhydene.2018.09.061

[17] Ni M, Leung MKH, Leung DYC. Parametric study of solid oxide fuel cell performance. Energy Convers Manage. 2007;48:1525-35. https://doi.org/10.1016/j.enconman.2006.11.016

[18] Xie J, Hao W, Wang F. Analysis of anode functional layer for minimizing thermal stress in solid oxide fuel cell. Appl Phys A. 2017;123. https://doi.org/10.1007/s00339-017-1266-x

[19] Schlegl H, Dawson R. Finite element analysis and modelling of thermal stress in solid oxide fuel cells. Proc Inst Mech Eng Part A J Power Eng. 2017;231:654-65. https://doi.org/10.1177/0957650917716269

[20] Wang C, Yang J, Huang W, Zhang T, Yan D, Pu J, et al. Numerical simulation and analysis of thermal stress distributions for a planar solid oxide fuel cell stack with external manifold structure. Int J Hydrogen Energy. 2018;43:20900-10. https://doi.org/10.1016/j.ijhydene.2018.08.076

[21] Jiang TL, Chen M-H. Thermal-stress analyses of an operating planar solid oxide fuel cell with the bonded compliant seal design. Int J Hydrogen Energy. 2009;34:8223-34. https://doi.org/10.1016/j.ijhydene.2009.07.089

[22] Xu M, Li T, Yang M, Andersson M. Solid oxide fuel cell interconnect design

optimization considering the thermal stresses. Sci Bull. 2016;61:1333-44. https://doi.org/10.1007/s11434-016-1146-3

[23] Zeng S, Yu G, Parbey J, Song D, Li T, Andersson M. Effect of the Electrochemical Active Site on Thermal Stress in Solid Oxide Fuel Cells. J Electrochem Soc. 2018;165:F105-F13. https://doi.org/10.1149/2.1341802jes

[24] Peksen M. 3D transient multiphysics modelling of a complete high temperature fuel cell system using coupled CFD and FEM. Int J Hydrogen Energy. 2014;39:5137-47. https://doi.org/10.1016/j.ijhydene.2014.01.063

[25] Fang X, Lin Z. Numerical study on the mechanical stress and mechanical failure of planar solid oxide fuel cell. Appl Energy. 2018;229:63-8. https://doi.org/10.1016/j.apenergy.2018.07.077

[26] Bove R, Ubertini S. Modeling solid oxide fuel cells: methods, procedures and techniques: Springer Science & Business Media; 2008.

[27] Zeng S, Zhang X, Song Chen J, Li T, Andersson M. Modeling of solid oxide fuel cells with optimized interconnect designs. Int J Heat Mass Transfer. 2018;125:506-14. https://doi.org/10.1016/j.ijheatmasstransfer.2018.04.096

[28] Xu H, Chen B, Liu J, Ni M. Modeling of direct carbon solid oxide fuel cell for CO and electricity cogeneration. Appl Energy. 2016;178:353-62. https://doi.org/10.1016/j.apenergy.2016.06.064

[29] Chaudhary TN, Saleem U, Chen B. Reacting flow coupling with thermal impacts in a single solid oxide fuel cell. Int J Hydrogen Energy. 2019;44:8425-38. https://doi.org/10.1016/j.ijhydene.2019.02.043

[30] Pianko-Oprych P, Zinko T, Jaworski Z. A Numerical Investigation of the Thermal Stresses of a Planar Solid Oxide Fuel Cell. Materials. 2016;9:814. https://doi.org/10.3390/ma9100814

[31] Stevenson JW, Armstrong TR, Carneim RD, Pederson LR, Weber WJ. Electrochemical properties of mixed conducting perovskites La(1-x)M(x)Co(1-y)Fe(y)O(3-delta) (M=Sr,Ba,Ca). J Electrochem Soc. 1996;143:2722-9. https://doi.org/10.1149/1.1837098

[32] Xu H, Chen B, Tan P, Cai W, He W, Farrusseng D, et al. Modeling of all porous solid oxide fuel cells. Appl Energy. 2018;219:105-13. https://doi.org/10.1016/j.apenergy.2018.03.037

[33] Zeng S, Xu M, Parbey J, Yu G, Andersson M, Li Q, et al. Thermal stress analysis of a planar anode-supported solid oxide fuel cell: Effects of anode porosity. Int J Hydrogen Energy. 2017;42:20239-48. https://doi.org/10.1016/j.ijhydene.2017.05.189

[34] Hussain M, Li X, Dincer I. A numerical investigation of modeling an SOFC electrode as two finite layers. Int J Hydrogen Energy. 2009;34:3134-44. https://doi.org/10.1016/j.ijhydene.2009.01.049

[35] Yang F, Gu JM, Ye LH, Zhang ZX, Rao GF, Liang YC, et al. Justifying the significance of Knudsen diffusion in solid oxide fuel cells. Energy. 2016;95:242-6. https://doi.org/10.1016/j.energy.2015.12.022

[36] Yakabe H, Hishinuma M, Uratani M, Matsuzaki Y, Yasuda I. Evaluation and modeling of performance of anode-supported solid oxide fuel cell. J Power Sources. 2000;86(1):423-31. https://doi.org/10.1016/S0378-7753(99)00444-9

[37] Chan SH, Khor KA, Xia ZT. A complete polarization model of a solid oxide fuel cell and its sensitivity to the change of cell component thickness. J Power Sources. 2001;93(1-2):130-40. https://doi.org/10.1016/S0378-7753(00)00556-5

[38] Zhang Z, Yue D, Yang G, Chen J, Zheng Y, Miao H, et al. Three-dimensional CFD modeling of transport phenomena in multi-channel anode-supported planar SOFCs. Int J Heat Mass Transfer. 2015;84:942-54. https://doi.org/10.1016/j.ijheatmasstransfer.2015.01.097

[39] Kuang ZB. Theory of electroelasticity: Springer; 2013.

[40] Molla TT, Kwok K, Frandsen HL. Modeling the Mechanical Integrity of Generic Solid Oxide Cell Stack Designs Exposed to Long-term Operation. Fuel Cells. 2018;19:96-109. https://doi.org/10.1002/fuce.201800081

[41] Frandsen HL, Makowska M, Greco F, Chatzichristodoulou C, Ni DW, Curran DJ, et al. Accelerated creep in solid oxide fuel cell anode supports during reduction. J Power Sources. 2016;323:78-89. https://doi.org/10.1016/j.jpowsour.2016.04.097

[42] Xu M, Li TS, Yang M, Andersson M, Fransson I, Larsson T, et al. Modeling of an anode supported solid oxide fuel cell focusing on thermal stresses. Int J Hydrogen Energy. 2016;41:14927-40. https://doi.org/10.1016/j.ijhydene.2016.06.171

[43] Masini A, Šiška F, Ševeček O, Chlup Z, Dlouhý I. Elastic properties of multi-layered ceramic systems for SOCs. Int J Appl Ceram Technol. 2018;15:370-9. https://doi.org/10.1111/ijac.12801